

CoFe₂O₄@N-CNH as Bifunctional Hybrid Catalysts for Rechargeable Zinc-Air Batteries

Sudheer Kumar Yadav, Daniel Deckenbach, Sandeep Yadav, Christian Njel, Vanessa Trouillet, and Jörg J. Schneider*

Improving the efficiency of bifunctional electrocatalysts is a decisive challenge in the area of long-lasting rechargeable zinc-air batteries. Enhancing the catalysts' performance is crucial for advancing zinc-air batteries.

Transition-metal oxides have emerged as promising non-precious, noble-metal-free catalysts. Herein, a unique precursor directed approach is introduced for preparing a cobalt ferrite@nitrogen doped carbon nanohorns (CoFe₂O₄@N-CNHs) nanohybrid catalyst in a single step annealing process involving stoichiometric amounts of single-source cobalt and iron molecular precursors and carbon nanohorns (CNHs) under an argon/ammonia (Ar/NH₃) atmosphere. This procedure enables a simultaneous CoFe₂O₄ ferrite synthesis and nitrogen functionalization of CNHs. The precious metal free nanohybrid CoFe₂O₄@N-CNHs-30% containing 30% of carbon presents an oxygen reduction reaction (ORR) half wave potential and onset potential comparable to the standard ORR catalyst 20% Pt/C. CoFe₂O₄@N-CNHs-30% also establishes superior oxygen evolution reaction (OER) performance with a low overpotential and a small Tafel slope than benchmark OER catalyst RuO₂. Furthermore, the rechargeable zinc-air battery with the CoFe₂O₄@N-CNHs-30% nanohybrid as air electrode demonstrates steadier and more durable charge–discharge cycles, and outstanding energy density relative to the state-of-the-art 20% Pt/C-RuO₂ catalyst.

1. Introduction

Rechargeable metal-air batteries have allured renewed focus in recent years as a feasible energy storage solution. With an ample oxygen supply from the surroundings, metal-air batteries have a remarkably higher theoretical energy density than conventional batteries. Amidst numerous other metal-air batteries (lithium-air, sodium-air, potassium-air, aluminum-air, and magnesium-air batteries),^[1] the zinc-air battery has been deemed an appealing possibility due to its distinct advantages, such as security, low price, and environmental friendliness. It has also been proposed as a potential metal-air system for realistic application scenarios. Primary zinc-air batteries are currently employed in various medical and telecommunications applications, including hearing aids and wireless messaging systems.^[2] On the other hand, the absence of long-lasting air catalysts and zinc anodes with high cyclability has hindered the growth of rechargeable secondary zinc-air batteries so far.^[3] The sluggish oxygen reduction reaction (ORR) and the oxygen evolution

reaction (OER) kinetics of air catalysts lead to large overpotentials and considerable energy and efficiency loss.^[4–6] The active noble metal containing catalysts, for example, Pt for ORR and IrO₂ or RuO₂ for OER, are ineffective as bifunctional catalysts in catalyzing ORR/OER in metal-air batteries. Furthermore, their inconstant activity and high cost hinder the commercialization of metal-air batteries with such catalysts. As a result, a great deal of attention has been paid to the development of innovative bifunctional electrocatalysts with efficient electrocatalytic activity, which could considerably lower the overpotential and improve cyclic stability in the direction of realizing a rechargeable zinc-air battery. There have been recognizable developments in evolving low-priced and highly active bifunctional electrocatalysts, particularly transition metal oxide composites with heteroatom-doped carbonaceous materials having better activity than noble metal catalysts.^[7] Nitrogen doping (N-doping) induces polarization of carbon atoms which leads to change in charge density along the framework without distraction of the π electron system of the carbon host.^[7] Thus, N-doping generates electronically

S. K. Yadav, D. Deckenbach, S. Yadav, J. J. Schneider
Fachbereich Chemie
Eduard-Zintl-Institut für Anorganische und Physikalische Chemie
Technische Universität Darmstadt
Peter-Grünberg-Strasse 12, Darmstadt 64287, Germany
E-mail: joerg.schneider@tu-darmstadt.de

C. Njel, V. Trouillet
Institute for Applied Materials (IAM-ESS) and Karlsruhe Nano Micro Facility (KNMF), Karlsruhe Institute of Technology (KIT)
Karlsruhe Institute of Technology (KIT)
Hermann-von-Helmholtz-Platz 1, Eggenstein-Leopoldshafen 76344, Germany

 The ORCID identification number(s) for the author(s) of this article can be found under <https://doi.org/10.1002/admi.202400415>

© 2024 The Author(s). Advanced Materials Interfaces published by Wiley-VCH GmbH. This is an open access article under the terms of the [Creative Commons Attribution](#) License, which permits use, distribution and reproduction in any medium, provided the original work is properly cited.

DOI: 10.1002/admi.202400415

modified active sites (C-N) and enhances the coordination of oxygen and transfer of electrons during the ORR and OER processes.^[8] Moreover, transition metal oxides allured notable attention due to availability, price, electrochemical durability, and satisfactory ORR and OER catalytic ability.^[9] Among them, spinel oxides are widely investigated due to their straightforward synthesis, modifiable chemical constitution, and structural heterogeneity.

Also, it is postulated that in spinels, the cations in octahedral sites operate as active centers for ORR/OER. Thus the e_g orbital filling of these active cations in the octahedral sites seems to be the activity descriptor for ORR/OER.^[10,11] Spinel oxides are typically combined with a conducting support, for example, a carbon framework, to guarantee quick electron transport. Additionally, the support framework is crucial for the mass transport in the triple phase regions (solid-liquid-gas) needed for ORR and OER. CoFe_2O_4 a part of bimetal spinel oxides $\text{M}_x\text{Fe}_{3-x}\text{O}_4$ (where M is a transition metal, for example, Co, Fe, Ni, Zn, Mn), anchored on N-doped carbon matrix, have attracted interest in the study of their ORR/OER activity.^[10,12,13] Nanonano-hybrids such as $\text{Co}/\text{CoFe}_2\text{O}_4@\text{N}$ -graphene, $\text{CoFe}_2\text{O}_4@\text{N}/\text{S}$ -copolydoped mesoporous carbon spheres, $\text{CoFe}_2\text{O}_4@\text{N}$ -graphene oxide, Zr doped $\text{CoFe}_2\text{O}_4@\text{N}$ -graphene oxide, $\text{CoFe}/\text{COFe}_2\text{O}_4@\text{N}$ -CNT and $\text{CoFe}_2\text{O}_4@\text{N}$ -carbon nanofibers has been already reported as ORR/OER bifunctional electrocatalysts.^[5,10,12,14–16]

Thus, distinct carbon supports such as carbon nanotubes (CNTs), graphene, and carbon nanofibers have been documented to improve air electrode performances. This is attributed to the enhanced mass transfer due to their distinctive structural framework.^[17] Recently, carbon nanohorns (CNHs),^[18] in particular, have been presented as potential materials as electrocatalysts in fuel cells, oxygen reduction, water splitting, and electrochemical bio-sensing.^[14,15,19,20] The bud-like CNHs which have been used in this study have a limited surface area and pore volume due to their entangled structure and closed single wall topologies. However, when CNHs are subjected to annealing in the presence of gases like O_2 , CO_2 , N_2 , or NH_3 gas, it results in CNH functionalization as well as the formation of nanochannels within the CNHs.^[19,21,22] Additionally, annealing can induce the creation of defects and voids as well as the opening of the end tips in the nanohorns, thereby further enhancing the porosity, and modifying charge transfer capabilities, and conductivity of CNHs.

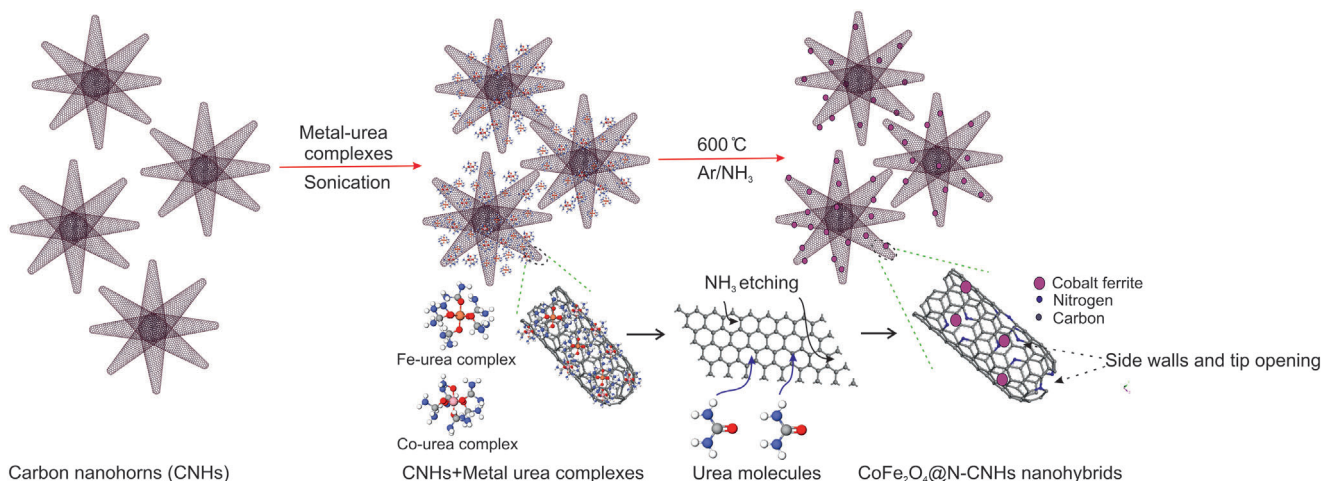
This work reports a straightforward and novel approach for the synthesis of spinel CoFe_2O_4 nanoparticles anchored on N-functionalized carbon nanohorns ($\text{CoFe}_2\text{O}_4\text{-N}@\text{CNHs}$) as a promising bifunctional electrocatalyst. The $\text{CoFe}_2\text{O}_4@\text{N}$ -CNHs nanohybrid catalyst is prepared by a controlled thermal conversion of stoichiometric amounts of single-source molecular precursors based on cobalt urea nitrate (Co-urea) and iron urea nitrate (Fe-urea) complexes that are tethered to CNHs in an argon/ammonia (Ar/NH_3) atmosphere. The Fe-urea nitrate and Co-urea nitrate complexes act as nitrogen and oxygen sources in this process. As a result, active nitrogen species such as pyridinic nitrogen (pyridinic N) and quaternary nitrogen (quaternary N) centers are formed which mediate a metal coordination with nitrogen of type $[\text{M}-\text{N}_x]$ in the carbon matrix. Furthermore, when iron and cobalt molecular precursors are combined in nitrogen-doped carbon materials, they can spontaneously cre-

ate CoFe_2O_4 spinel oxide.^[23] Additionally, NH_3 etching plays a pivotal role in the following aspects: (i) Increasing porosity and specific surface area of CNHs due to a selective etching of the CNH tips and framework and (ii) improving the total nitrogen content.^[7,19,24] This procedure is unique because it simultaneously leads to CoFe_2O_4 formation and N-functionalization or N-doping of CNHs. The schematic of the overall process is elucidated in **Scheme 1**. The nanohybrid $\text{CoFe}_2\text{O}_4@\text{N}$ -CNHs show better ORR and OER activity as compared to individual components as well as a nanohybrid composed of CoFe_2O_4 nanoparticles and N-CNHS prepared by a standard co-precipitation method. Our approach has the potential to be developed for other metal urea precursors^[25] allowing to broaden this synthetic route to a wide variety of metal oxides and oxidic spinels.

2. Results and Discussion

Iron urea nitrate $[\text{Fe}(\text{NH}_2\text{CONH}_2)_6(\text{NO}_3)_3]$ and cobalt urea nitrate complexes $[\text{Co}(\text{NH}_2\text{CONH}_2)_6(\text{NO}_3)_2]$ are synthesized by the precipitation method.^[26] The purity of the complexes is determined by FT-IR and thermogravimetric analysis (Figure S1, Supporting Information). To determine the suitable decomposition process leading to the formation of the cobalt ferrite a thermogravimetric analysis of a 1:2 mixture of the Co-urea and the Fe-urea complex allows insight. The physical mixture decomposition begins at 133 °C with mass loss of 85% up to 225 °C. Afterward, there is a further loss of 4% up to 450 °C until the constant mass reaches 10.6%. Thus, the primary decomposition phase of the mixture of the cobalt and iron urea complexes is between 200 and 450 °C, and the final and sole product obtained is CoFe_2O_4 . Based on a thermogravimetric analysis of the mixture of complexes, a T_{decomp} of 600 °C is chosen as the optimum reaction temperature for both nitrogen functionalization and efficient NH_3 based etching of CNHs,^[19] allowing a simultaneous formation of the final nanohybrid catalyst $\text{CoFe}_2\text{O}_4@\text{N}$ -CNHs.

Thus, N-functionalized CNHs/cobalt ferrite nanoparticles ($\text{CoFe}_2\text{O}_4@\text{N}$ -CNHs) has been synthesized by thermal conversion of the two precursor mixtures with CNHs (see Experimental Section). Four samples identified as $\text{CoFe}_2\text{O}_4@\text{N}$ -CNHs-10%, $\text{CoFe}_2\text{O}_4@\text{N}$ -CNHs-30%, $\text{CoFe}_2\text{O}_4@\text{N}$ -CNHs-50%, and $\text{CoFe}_2\text{O}_4@\text{N}$ -CNHs-80%, based on the actual percentage of carbon content obtained from thermogravimetric analysis (in O_2) are synthesized (**Figure 1a**). Thermogravimetric analysis (in O_2) of pristine CNHs shows a single step 100% mass loss starting from 210 to 570 °C, confirming its purity and absence of any graphitic impurity.^[27] In TGA study of all the $\text{CoFe}_2\text{O}_4@\text{N}$ -CNHs nanohybrids, there are two significant mass loss steps. The first step of mass loss starts $\approx 260\text{--}270$ °C with a sharp major loss due to combustion of CNHs. A second mass loss occurs up temperatures of 600 °C and can be attributed to the combustion of graphitic structures, which are formed during annealing and formation of the $\text{CoFe}_2\text{O}_4@\text{N}$ -CNHs nanohybrids. Compared to the pristine CNHs, the stability of $\text{CoFe}_2\text{O}_4@\text{N}$ -CNHs nanohybrid is weaker and is mainly governed by the ferrite/CNH interaction within the $\text{CoFe}_2\text{O}_4@\text{N}$ -CNHs-50%, hybrid. Weight loss thus begins at a lower temperature than in the pure CNH sample or the pure ferrite due to this weaker interaction of the ferrite and the CNH carbon surface in the nanostructured hybrid representing the initial decomposition site.



Scheme 1. Schematic illustration exemplifying the synthesis of the bifunctional composite catalyst $\text{CoFe}_2\text{O}_4@N\text{-CNHs}$, employing the molecular cobalt and iron urea complexes ($\text{Co}(\text{NH}_2\text{CONH}_2)_6(\text{NO}_3)_2$ and $\text{Fe}(\text{NH}_2\text{CONH}_2)_6(\text{NO}_3)_3$) as molecular precursors.

Powder X-ray diffraction (XRD) patterns of the $\text{CoFe}_2\text{O}_4@N\text{-CNHs}$ nanohybrids are assigned to the cubic spinel phase of CoFe_2O_4 (PDF#22-1086), apart from the one broad peak at $\approx 2\text{-}\theta^\circ$ of 26° , which matches with the (002) peak of graphitic car-

bon in CNHs (Figure 1b). The mean crystallite size of CoFe_2O_4 is estimated to be 10.0 nm using Scherer's equation whereas it is between 5 and 8 nm in $\text{CoFe}_2\text{O}_4@N\text{-CNHs}$ nanohybrids. The decrease in crystallite size in the nanohybrids is obviously due to the presence of CNHs, which act as a homogeneous diluting matrix during spinel formation. The metal urea nitrate precursors are thus well dispersed on the CNHs matrix forming small crystallites.

The structure and morphology of pristine CNHs, N-CNHS, pure CoFe_2O_4 nanoparticles, and $\text{CoFe}_2\text{O}_4@N\text{-CNHs}$ nanohybrids have been explored by transmission electron microscopy (TEM) and field emission scanning electron microscopy (FE-SEM). The CNH particles exhibit a bud-like spherical structure (TEM, Figure S2, Supporting Information). After NH_3 treatment, CNHs did not reveal any significant morphological changes (Figure 2a). In TEM CoFe_2O_4 nanoparticles exhibit an irregular structure with an average size of ≈ 8.9 nm (Figure 2b, particle size distribution, Figure S3a, Supporting Information). Electron microscopy (FE-SEM) of the CoFe_2O_4 nanoparticles shows large clusters due to aggregation (Figure S4b, Supporting Information). TEM images of $\text{CoFe}_2\text{O}_4@N\text{-CNHs}$ nanohybrids however exhibit a uniform distribution of CoFe_2O_4 nanoparticles over carbon nanohorns (Figure 2c-f). The average particle size of CoFe_2O_4 nanoparticles in the nanohybrids varies from ≈ 7 to 10 nm (particle size distribution, Figure S3b-e, Supporting Information). The FE-SEM of nanohybrids depicts a spherical morphology (Figure S4c-f, Supporting Information). Elemental mapping confirms the presence and homogeneous distribution of cobalt, iron, carbon, nitrogen, and oxygen in these nanohybrids. Notably, the bud-like spherical structure of N-CNHS and nanohybrids remains stable even after annealing. Retention of this morphology of the CNHs improves the electric connection between CoFe_2O_4 nanoparticles allows a good active mass transport due to the macro sized dimensions between the bud like CNH aggregates and enhances catalytic capabilities.^[28,29] HRTEM of the CNHs confirms their bud-like morphology. The characteristic conical tip structure of an isolated CNH cone protruding out of bundle has a length of ≈ 5 nm and a diameter of 2–3 nm (Figure S5a, Supporting Information).^[30] The HRTEM images

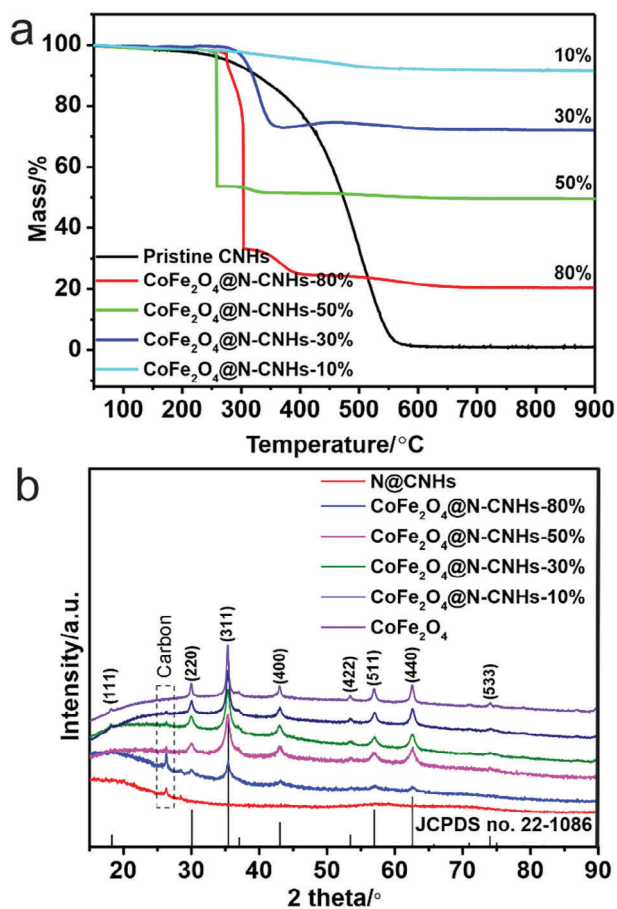


Figure 1. a) Thermogravimetric analysis and b) X-ray diffraction (XRD) pattern of $\text{CoFe}_2\text{O}_4@N\text{-CNHs}$ nanohybrids.

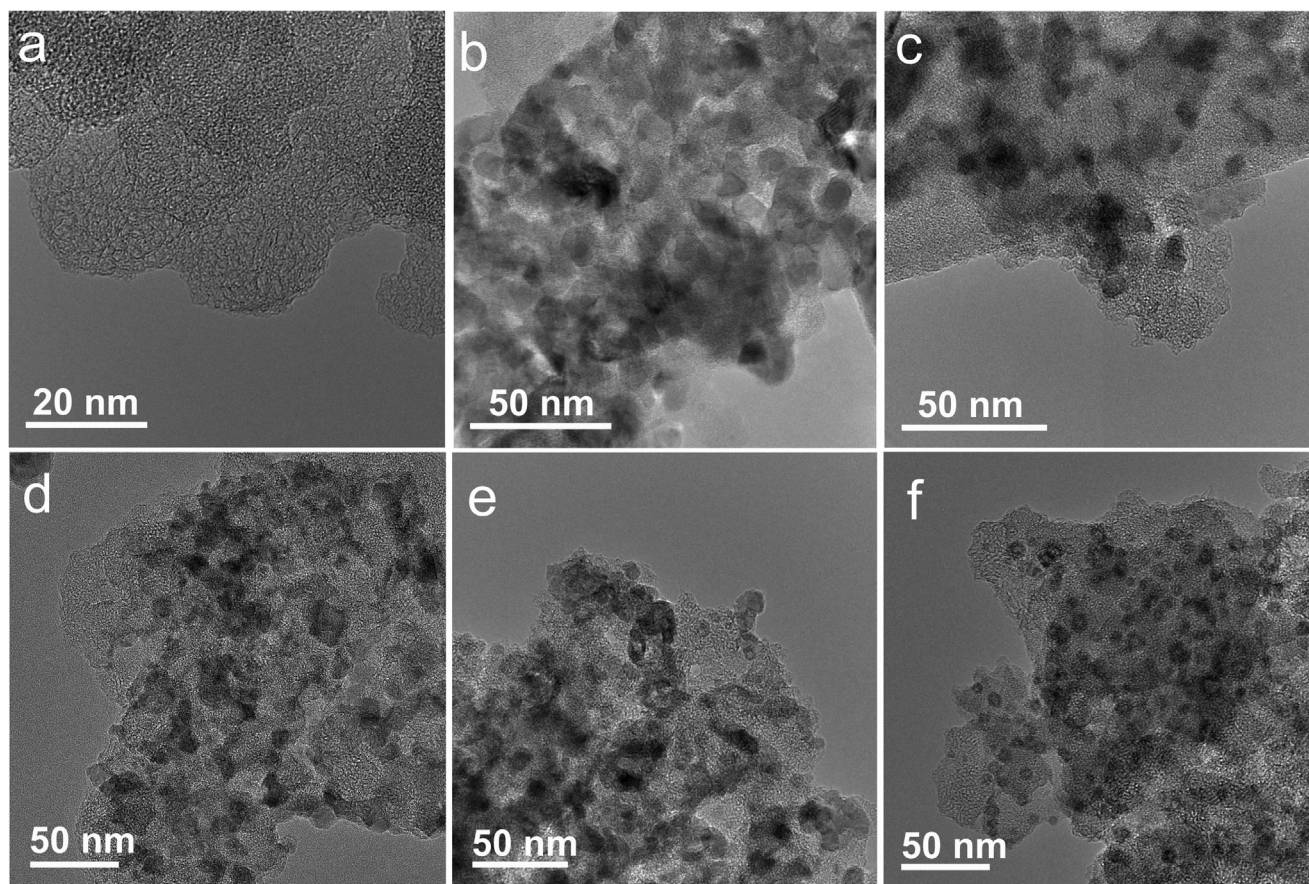


Figure 2. TEM images of a) bud-like N-CNHs, b) bare CoFe_2O_4 nanoparticles and CoFe_2O_4 @N-CNHs nanohybrids c)–10%, d)–30%, e)–50% and f)–80%.

for the nanohybrids display CoFe_2O_4 nanoparticles tethered onto the surface of CNHs. The efficient connection between CoFe_2O_4 and CNHs is proven by XRD. The (311), (400), (422), (440), and (620) planes of spinel CoFe_2O_4 can be recognized in the HRTEM image of pure CoFe_2O_4 (Figure S5b, Supporting Information). In the nanohybrids (Figure S5c–f, Supporting Information) the SAED pattern planes are assigned to (220), (311), (222), (331), (440), and (620) of the CoFe_2O_4 spinel.

Raman spectroscopy provided compelling indications of both, surface defects generated on the nanohorns and the introduction of nitrogen dopants into the CNHs framework structure (Figure S6, Supporting Information). The Raman spectrum of the pristine CNHs showed two broad peaks ≈ 1580 and 1330 cm^{-1} (Figure S6a, Supporting Information). The ratio (I_D/I_G) of the integrated areas of the D band to the G band is correlated to the degree of disorderness in carbon materials.^[22] The I_D/I_G ratios increases in the nanohybrids (Figure S6b, Supporting Information) as compared to pristine CNHs, in the order: CNHs (1.64) < N-CNHs (1.74) < CoFe_2O_4 @N-CNHs-80% (1.83) < CoFe_2O_4 @N-CNHs-10% (1.91) < CoFe_2O_4 @N-CNHs-50% (1.95) < CoFe_2O_4 @N-CNHs-30% (1.99). These results clearly indicate that nanohybrids have the highest degree of disorder due to significant defects created by NH_3 -etching on the CNHs matrix. Additionally, during pyrolysis, urea complex combustion also promoted the etching and N-doping of CNHs.^[7] The

created defect sites together with the N-doping provide highly active centers for the ORR. N-doping of CNHs is also confirmed by a shift in the G band and 2D band position to a higher wave number in N-CNHs and the nanohybrids (Table S1, Supporting Information). It is documented that the electron-withdrawing impact of nitrogen doping in the carbon framework causes a redshift in the G-band and 2D band position.^[31,32] In the Raman spectra of the nanohybrids, three signals at 312 , 470 , and 677 cm^{-1} correspond to phonon modes of the spinel cobalt ferrite.^[33] The relative intensity of these three bands increases with CoFe_2O_4 content in the nanohybrids (Figure S6b, Supporting Information).

Nitrogen adsorption isotherms allow insight into the porosity of the nanohybrids. (Figure 3a). All the nanohybrids and CNHs showed Type-IVa isotherms with an apparent hysteresis loop at medium relative pressure, revealing a dominant mesoporous structure. An increasing tendency in N_2 adsorption is noticed for nanohybrids relative to pristine CNHs, indicating significant increase in surface area after NH_3 -based thermal annealing. The pristine CNHs show a BET surface area of $199.01\text{ m}^2\text{ g}^{-1}$, which increases to $359.9\text{ m}^2\text{ g}^{-1}$ for N-CNHs, $260.2\text{ m}^2\text{ g}^{-1}$ for CoFe_2O_4 @N-CNHs-10%, $387.2\text{ m}^2\text{ g}^{-1}$ for CoFe_2O_4 @N-CNHs-30%, $395.0\text{ m}^2\text{ g}^{-1}$ for CoFe_2O_4 @N-CNHs-50%, and $425.6\text{ m}^2\text{ g}^{-1}$ for CoFe_2O_4 @N-CNHs-80%. N-CNHs reveal a twofold increase in the surface area compared to the pristine CNHs due to the NH_3 mediated etching of the framework. All the nanohybrids

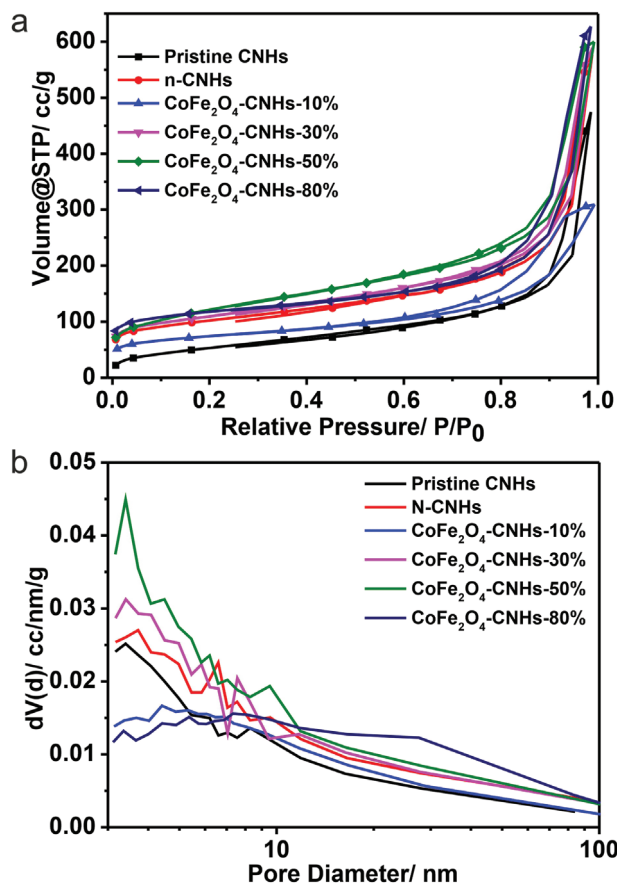


Figure 3. a) Nitrogen adsorption isotherm, and b) BJH pore size distribution of pristine CNHs, N-CNHs, and the CoFe_2O_4 @N-CNHs nanohybrids.

also show enhancements in the surface area and N_2 adsorption isotherm except the one with only 10% CNHs content.^[22] Using the BJH and t-plot methods the pore size distribution for all the samples were determined (Figure 3b; Table S2, Supporting Information). For the CNHs, different types of pores exist: micropores (<2 nm) consisting of interlayer space between graphene sheets (core micropores) and interstitial spaces between adjacent nanohorns (interstitial-micropores), the mesopores (2–5 nm) in the internal space of the nanohorns, and finally macropores (5–100 nm) which exist between larger aggregates of the CNHs.^[34] The pore size distribution profile corresponding to pristine CNHs reveals the presence of mesopores, with apparently no indication of microporosity (Figure 3b and Table S2, Supporting Information).

The pore size distribution for pristine CNHs present a few inflection points. However, the nanohybrids present many inflection points and this is because of modification of mesopores structures due to heat treatment in the presence of NH_3 (etching) and urea complexes (combustion). Mesopores and micropores creation of different sizes is the reason of these inflections in the nanohybrids attributed to the availability of the internal tube space through the opening at the tip or surface of the nanohorns and etching of carbon impurities in spaces between the spherical nanohorn particles.^[7,19,35]

The pore size of N-CNHs and nanohybrids are within the size range of 3.1 to 100 nm, with a maximum density between 3.5 and 7.3 nm. It indicates that most of the pores on nanohybrids and N-CNHs are mesopores and macropores.^[19] Moreover, insights from nitrogen sorption and t-plot outcomes (see Figure S7a and Table S2, Supporting Information) unequivocally demonstrate that nanohybrids manifest an increased number of micropores. This phenomenon effectively enhances the active reaction site density, thereby facilitating the promotion of ORR through the establishment and accessibility of suitable C-N active sites.^[7] The creation of micropores in CNHs after heat treatment in the presence of NH_3 is also evident from previous reports.^[19,28,32] The cumulative pore volume, microporous surface area, and pore volume increases in N-CNHs and nanohybrids compared to pristine CNHs (Figure S7a and Table S2, Supporting Information). Along with the creation of microporosity, there is also an enhancement in pore volume of meso/macropores in N-CNHs and nanohybrids. This increase is accredited to the availability of the internal CNHs tube space through the opening at the tip or surface of the nanohorns and etching of carbon impurities in spaces between the spherical nanohorn particles.^[19] In support of the above statement, Figure S7b,c (Supporting Information) exhibits comparative TEM images of nanohorn conical tip structures for the pristine CNHs and the nanohybrid CoFe_2O_4 @N-CNHs-30%, respectively. Conical tip opening is apparent in all of the nanohybrids. This is attributed to the heat treatment procedure of CNHs in the presence of metal urea nitrate complexes and NH_3 . Especially the nitrate anion is known to act as an oxidizer under such thermal conditions. Overall, formation of such defined porous structures in the CNHs will significantly enhance mass transport phenomena and enhances the durability of the nanohybrids toward their ORR and OER activity. In general, micropores are responsible for high surface area and adsorption capacity. Mesopores density helps uncover more active sites along with better diffusion of reactants, and the macropores could act as host void space serving as larger reservoirs. Thus, the textural and morphological characteristics of the nanohybrids support an improved bifunctional activity compared to the isolated components alone.

Chemical characterization of pristine CNHs and CoFe_2O_4 @N-CNH hybrids is done by XP spectroscopy. For pristine CNHs signals for C1s, N1s, O1s, C KLL, and O KLL confirm the purity of the CNHs except for the presence of a very minor amount of nitrogen contamination (Figure S8a, bottom, Supporting Information). High-temperature NH_3 treatment of the CNHs resulting in N-CNHs leads to a significant reduction of the oxygen content (Figure S8a, top, Supporting Information). N-CNHs lose some oxygen functionalities, indicated by a decrease in the total amount of oxygen from 6.7 at% to 2.1 at% as obtained from the high energy resolution spectra and indicated from the C=O and C–O species.^[36] Noticeably a decrease in the intensity of the carbonaceous contamination (sp^3) and of the already very weak oxygenated carbon species is furthermore observed (Figure S8b,c, Supporting Information). Figure 4a represents the survey spectra of CoFe_2O_4 @N-CNHs nanohybrids showing the existence of C, N, O, Co, and Fe without other elemental impurities. In the high-resolution spectra of CoFe_2O_4 @N-CNHs-30% nanohybrids the C1s spectrum (Figure 4b) shows contributions with binding energies at 284.4 eV attributed to graphitic sp^2 carbon, 285.0 eV due to C–C bonds (sp^3 carbon). The signal at a binding energy

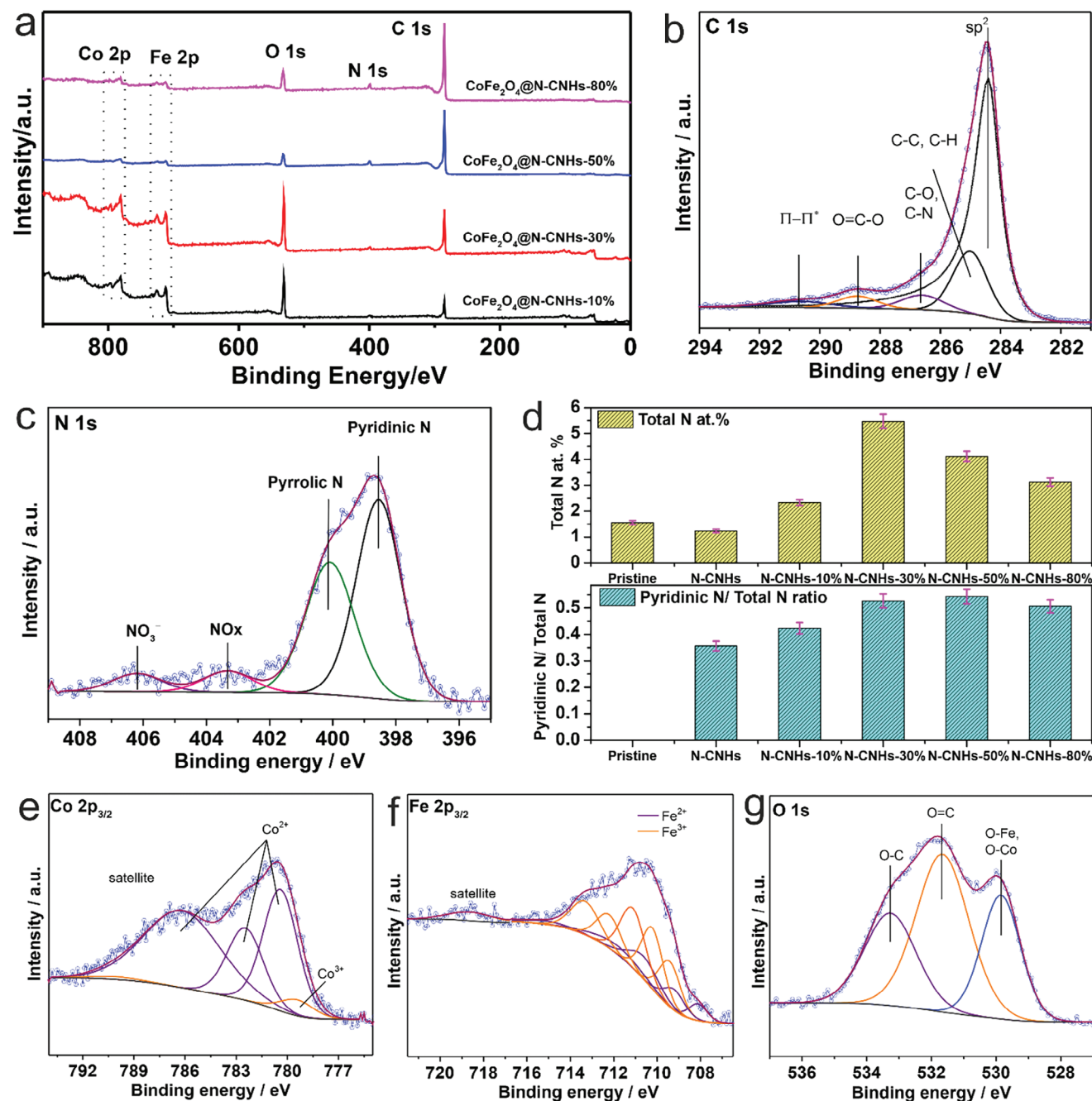


Figure 4. a) XPS survey spectra of the $\text{CoFe}_2\text{O}_4@N\text{-CNHs}$ nanohybrids. b) High-resolution XPS spectra of b) C 1s, c) N 1s, and d) the estimated value of different type nitrogen in all the samples. High-resolution XPS spectra of e) Co $2p_{3/2}$, f) Fe $2p_{3/2}$, and g) O 1s for the $\text{CoFe}_2\text{O}_4@N\text{-CNH-30\%}$ nanohybrid.

of 290.6 eV is attributed to $\pi\text{-}\pi^*$ excitations of the CNH matrix. Signals at binding energies of 286.6 and 288.8 eV can be ascribed to C–O/C–N, and O=C=O fragments, respectively. Additionally, the C–C and C–O are present on the nanohybrid surface, the fact that they are covered below the main signal suggests that their proportion is low compared to that of the contribution from the sp^2 carbon species. High-resolution N1s spectra of the N-CNHS (after heat treatment at 600 °C in Ar/ NH_3) reveal binding energies for pyridinic (398.5 eV), pyrrolic (400.1 eV), quaternary nitro-

gen (402.1 eV) and some oxidized species (trace amounts) (Figure 4c). Comparing the N1s peaks of all $\text{CoFe}_2\text{O}_4@N\text{-CNH}$ nanohybrids reveal different atomic ratios for the different N species present in the hybrids (Figure S9, Supporting Information). The pyridinic atomic ratio is shown in Figure 4d as well as the total amount of nitrogen.

Pristine CNHS possess a total nitrogen loading of 1.2 at%, which further increased in nanohybrids (2.6% to 5.47%). The nanohybrid $\text{CoFe}_2\text{O}_4@N\text{-CNHs-30\%}$ exhibits a maximum total

nitrogen content of 5.47% (Figure 4d). Compared to pristine CNHs, in the nanohybrids containing 10%, 30%, and 50% of carbon, pyridinic N and total nitrogen content improved due to the heat treatment of CNHs in the presence of metal urea nitrate complexes. It has been documented that heat treatment in the presence of urea induces pyridinic N-doping in CNHs.^[32] The pyridinic to total nitrogen content ratio variation of the different samples is in the order $\text{CoFe}_2\text{O}_4@\text{N-CNHS-50\%} \approx \text{CoFe}_2\text{O}_4@\text{N-CNHS-30\%} > \text{CoFe}_2\text{O}_4@\text{N-CNHS-80\%} > \text{CoFe}_2\text{O}_4@\text{N-CNHS-10\%} > \text{N-CNHS}$. The core-level $\text{Co}2\text{p}_{3/2}$ spectrum shows peaks located at 780.4 and 782.5 eV attributed to Co^{2+} , typically accompanied by a satellite peak at 786.2 eV. In addition, the peak at 779.5 eV reveals the presence of Co^{3+} species (Figure 4e) in a small amount.^[37] The $\text{Fe}2\text{p}_{3/2}$ spectrum (Figure 4f) can be fitted with two multiplets attributed to the major Fe^{3+} species (orange) accompanied by a small amount of Fe^{2+} (magenta).^[38] The transformation between redox couples $\text{Co}^{3+}/\text{Co}^{2+}$ and $\text{Fe}^{3+}/\text{Fe}^{2+}$ in the spinel ferrites is responsible for improving the catalytic activity.^[14,39] In the O1s spectra of the $\text{CoFe}_2\text{O}_4@\text{N-CNHS}$ nanohybrids the peak at 530.2 eV is attributed to the typical metal-oxygen bond (Figure 4g). The peak at 531.6 eV is attributed to the C=O and the peak at 533.8 eV is ascribed to the C—O groups.

Prior to the study of the $\text{CoFe}_2\text{O}_4@\text{N-CNHS}$ nanohybrids catalysts in a zinc-air battery set up, the nanohybrid catalysts undergo analysis to ascertain their bifunctional catalytic activity characteristics. The ORR electrochemical analysis of the nanohybrid catalyst evaluation is done using an rotating disc electrode (RDE) in an O_2 -saturated 0.1 M KOH electrolyte solution. The cyclic voltammetry (CV) curve of the $\text{CoFe}_2\text{O}_4@\text{N-CNHS-30\%}$ nanohybrid shows no peak in an Argon-saturated electrolyte, while a well-defined redox peak is visible at 0.69 V versus Hg/HgO in an O_2 -saturated electrolyte (Figure S10a, Supporting Information). The linear sweep voltammograms (LSVs) profiles have been recorded using RDE at various rotating rates ($\text{CoFe}_2\text{O}_4@\text{N-CNHS-30\%}$, Figure S10b, Supporting Information). The outcome demonstrates the enhancement in diffusion limiting current density depending on the increase of the rotational rate attributed to first-order reaction kinetics on the absorption of diffused O_2 and the acceleration of mass transport. To facilitate a more quantitative and comparative analysis of the samples' ORR characteristics, LSVs have been recorded by maintaining the rotation rate of the working electrode at 1600 rpm in an O_2 saturated 0.1 M KOH solution (Figure 5a).

The LSVs for pristine CNHs, N-CNHS, CoFe_2O_4 NPs, and 20% Pt/C have similar curve behavior. However, LSV curves for $\text{CoFe}_2\text{O}_4@\text{N-CNHS}$ nanohybrids behave differently. They all have a more positive current response. This phenomenon is due to the presence of transition metal oxides (ferrites) which possess a more remarkable ability to adsorb oxygen, thus presenting a better ORR activity.^[40,41] The LSVs retain the characteristic features corresponding to ORR however with a distinct difference in terms of the onset potential, half-wave potential, and diffusion limiting current density between the samples. From Figure 5a and Table S3 (Supporting Information), it can be observed that $\text{CoFe}_2\text{O}_4@\text{N-CNHS-30\%}$ exhibits excellent ORR performance (limiting current density = -6.51 mA cm^{-2} and half-wave potential ($E_{1/2}$) = 0.080 V), which is even superior to Pt/C (-5.70 mA cm^{-2} , 0.070 V). As exhibited in Figure 5a and Table S3 (Supporting Information), onset potential, half-wave potential,

and limiting current density of $\text{CoFe}_2\text{O}_4@\text{N-CNHS-30\%}$ nanohybrid is improved compared to N-CNHS, and pure CoFe_2O_4 NPs, as well as the other $\text{CoFe}_2\text{O}_4@\text{N-CNHS}$ nanohybrids having different CNH content, studied.

Tafel measurements allow additional insights into the kinetic mechanism of the ORR. The $\text{CoFe}_2\text{O}_4@\text{N-CNHS-30\%}$ nanohybrid display the lowest Tafel slope of 59.2 mV dec^{-1} among all the catalysts studied, including Pt/C (91.1 mV dec^{-1}), indicating the best ORR kinetics behavior over all other compositions (Figure 5b). Next, the OER activity of all samples is examined in 0.1 M KOH (Figure 5c). The OER potential at $j = 10 \text{ mA cm}^{-2}$ and the corresponding Tafel slope of $\text{CoFe}_2\text{O}_4@\text{N-CNHS-30\%}$ (0.70 V, 59.2 mV dec^{-1}) is comparable to the RuO_2 benchmark (0.67 V, 81.6 mV dec^{-1}) and is significantly better than those of other nanohybrids (Figure 5c,d; Table S4, Supporting Information). As shown in Table S4 (Supporting Information), the onset potential on $\text{CoFe}_2\text{O}_4@\text{N-CNHS-30\%}$ (0.37 V) is more positive than the RuO_2 standard catalyst (0.58 V). The overpotential (η) required for achieving a current density of 10 mA cm^{-2} is 336 mV for $\text{CoFe}_2\text{O}_4@\text{N-CNHS-30\%}$, which is better than the other nanohybrids and only slightly lesser than standard RuO_2 . Remarkably, at higher overpotential, the current density on $\text{CoFe}_2\text{O}_4@\text{N-CNHS-30\%}$ surpasses that obtained of the RuO_2 catalyst. This may originate from the higher surface area and an increased active site density of $\text{CoFe}_2\text{O}_4@\text{N-CNHS-30\%}$. To further confirm the efficiency of the transfer process in the nanohybrid samples, rotating ring-disk electrodes (RRDE) polarization curves have been collected (Figure 5e,f; Table S5, Supporting Information). In this process, $\text{CoFe}_2\text{O}_4@\text{N-CNHS-30\%}$ exhibits lesser hydrogen peroxide (2.2%) formation than the other nanohybrids. The converted electron transfer number is ≈ 3.95 for $\text{CoFe}_2\text{O}_4@\text{N-CNHS-30\%}$, indicating a nearly ideal ORR four electron pathway.

To apprehend the primary reasons for improved electrochemical performance, double-layer capacitance (C_{dl}) has been determined for catalysts $\text{CoFe}_2\text{O}_4@\text{N-CNHS-30\%}$, $\text{CoFe}_2\text{O}_4@\text{N-CNHS-50\%}$ and 20% Pt/C + RuO_2 (1:1) (Figure S11, Supporting Information). $\text{CoFe}_2\text{O}_4@\text{N-CNHS-30\%}$ exhibited the highest C_{dl} (35.4 mF cm^{-2}) and corresponding electrochemical surface area (ECSA) for $\text{CoFe}_2\text{O}_4@\text{N-CNHS-30\%}$ is higher than $\text{CoFe}_2\text{O}_4@\text{N-CNHS-50\%}$ and 20% Pt/C + RuO_2 catalysts. High ECSA values indicates accessibility of more active sites for electrochemical reactions, which contribute to an increase in electrocatalytic activity. EIS measurement (Nyquist plots) reports charge transfer resistance (R_{ct}) for $\text{CoFe}_2\text{O}_4@\text{N-CNHS-30\%}$ (70.5 Ohm) is smaller than $\text{CoFe}_2\text{O}_4@\text{N-CNHS-50\%}$ (76.6 Ohm) and 20% Pt/C + RuO_2 (81.5 Ohm). These findings suggest good conductivity and better faradaic reaction kinetics at electrode/electrolyte interface in case of $\text{CoFe}_2\text{O}_4@\text{N-CNHS-30\%}$ catalyst. The activity of the $\text{CoFe}_2\text{O}_4@\text{N-CNHS}$ for the ORR and OER rely on a synergistic interaction of the individual components, cobalt ferrite and N-doped carbon nanohorns. TEM studies confirm the uniform distribution of cobalt ferrite nanoparticles anchored over the porous carbon nanohorn matrix; the hybrid structure helps in exposing active sites, and enhances oxygen adsorption, mass transfer and electrolyte penetration.^[42] The N-doping persuade polarization of carbon atoms, change in charge density along the carbon network without the destruction of the π electron system in CNHs. Thus, N-doping creates electronically altered active C-N sites and enhances the coordination of oxygen and transfer of electrons

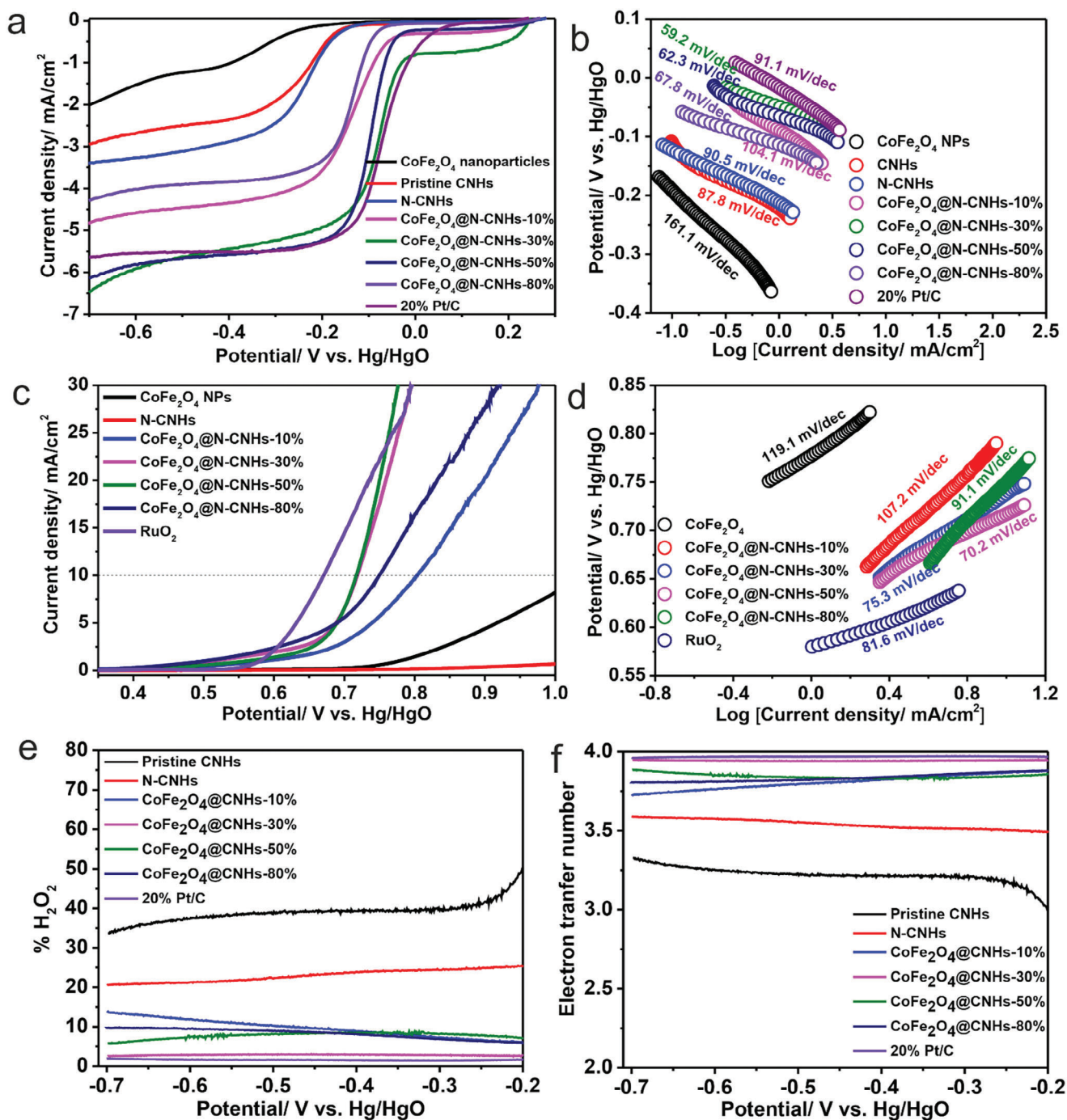


Figure 5. Electrochemical RDE and RRDE measurements: ORR characteristics a) LSV curves, and b) corresponding Tafel plot. c) OER measurements and d) corresponding Tafel plots, e) peroxide percentage (H₂O₂%), and f) the number of electron transferred.

during the ORR and OER processes. Furthermore, spinel oxides with structural defects, vacancies and redox couple interaction Fe³⁺/Fe²⁺ and Co³⁺/Co²⁺ has also been validated as a promising strategy for improving the catalytic activity.^[39,43] The spinel oxide species improves the adsorption and dissociation energy of oxygen related intermediate reactants. The concept is attributed to the extension of O—O and O—H bond lengths initiated by interaction between the transition metal oxide and reactants at the active

sites.^[44] Thus the interactions of the Fe³⁺/Fe²⁺ and Co³⁺/Co²⁺ redox couples, oxygen lattice vacancies, and multiple active surface sites, such as C-N and pyridinic N species, promotes the improvement of the catalytic activity. Overall, the efficient catalytic activity (ORR and OER) arises from the combination of the high surface area and the synergetic coupling between the enriched N-doped carbon nanohorns and CoFe₂O₄ nanoparticles.^[39,40,45] This facts are supported by an observation of less activity of the individual

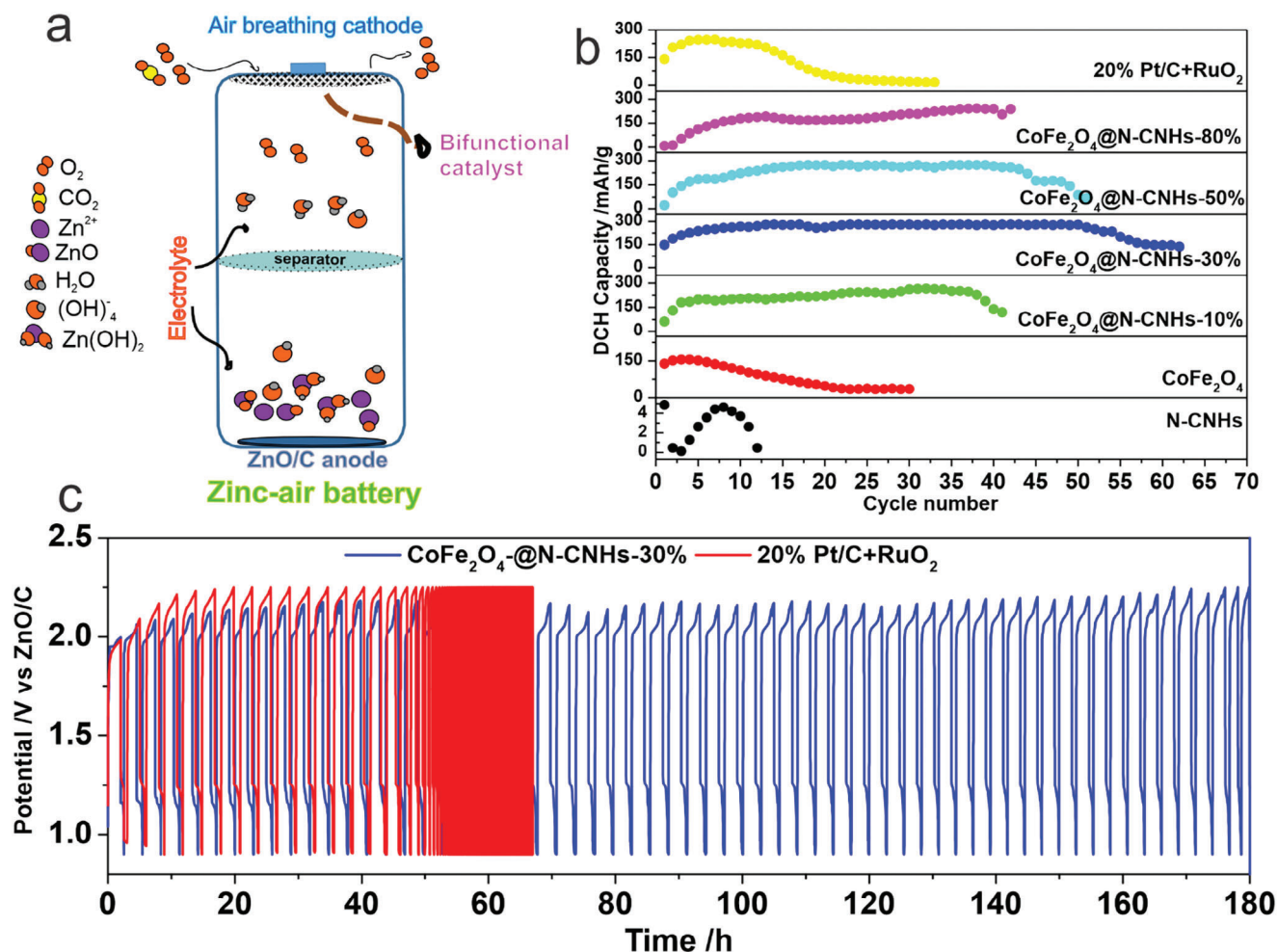


Figure 6. Schematic of a zinc-air battery set-up (a), Specific discharge capacity versus cycle number plot of all the samples, b) charge/discharge cyclization curves of CoFe₂O₄@N-CNHS-30% and 20% Pt/C + RuO₂ at the current density of 0.55 mA cm⁻² with 3 h per cycle.

components containing nanostructured CoFe₂O₄, CNHs, and N-CNHS combined in a nanocomposite CoFe₂O₄@N-CNHS prepared by the conventional co-precipitation method compared to the one reported herein.

Finally, a system level validation of the CoFe₂O₄@N-CNHS nanohybrid catalyst has been undertaken. A zinc-air battery has been set up using the CoFe₂O₄@N-CNHS-30% nanohybrid as catalyst as air cathode, a ZnO/C hybrid as anode, and a 4.0 M KOH as electrolyte (Figure 6a and Experimental Section for the fabrication of air electrodes, ZnO/C anode, and the complete zinc-air battery setup). The ZnO/C anode consists of ZnO nanoparticles integrated in a hierarchical porous carbon matrix, originating from the thermal decomposition of the ordered porous framework MOF-5 (Figure S12, Supporting Information). We have recently reported a MOF-5-derived ZnO/C anode and its utilization in rechargeable zinc-air batteries.^[46] This ZnO/C anode outperforms conventionally used zinc foil as anode. In this approach the real specific discharge capacity of the composite anode can be determined. This is different from most of the other studies with real Zinc-air cells because of the undefined excess anodic zinc reservoir which allows no proper balancing of

the cell characteristics. In addition, the ZnO/C anode displays an enhanced zinc availability realized by the distinctive 3D structure of the anode, which promotes improved zinc utilization. The ZnO/C composite anode enables reversible ZnO conversion by solving issues of ZnO dissolution, electrode passivation, and dendrite formation.^[46]

The performance of the zinc-air battery cell assembled with the 20% Pt/C + RuO₂ catalyst (Pt/C/RuO₂ = 1:1) is also evaluated under similar conditions for comparison. The initial open-circuit voltage of the zinc-air battery with CoFe₂O₄@N-CNHS-30% cathode is 1.10 V, which is comparable to those of a 20% Pt/C + RuO₂ conventional cathode (1.14 V). To further evaluate the catalytic stability, long-term galvanostatic charge-discharge of the Zinc-air battery using the CoFe₂O₄@N-CNHS-30% catalyst has been tested at a current density of 0.55 mA cm⁻². Figure 6b presents the variation of specific mean discharge capacity with the number of cycles at the current density of 0.55 mA cm⁻² for all samples. The charge voltage of the CoFe₂O₄@N-CNHS-30% equipped battery is ≈2.10 V, 0.15 V lower than for the 20% Pt/C + RuO₂ equipped battery (2.25 V). The voltage gap of battery devices with CoFe₂O₄@N-CNHS hybrids as cathode is smaller

in constant current discharge measurements, indicating its better rate proficiency.^[42] After continuous operation for over 180 h of charging and discharging, the voltage gap remained at the same level (Figure 6c). In comparison, 20% Pt/C + RuO₂ displayed rapid performance degradation after 48 h. The zinc-air battery based on the CoFe₂O₄@N-CNHs-30% cathode shows a better cycling performance in terms of depth of discharge (DOD) and discharge capacity retention (Table S6, Supporting Information). For each catalyst during the first 5–10 cycles, there is variation in specific capacity due to insufficient catalyst wetting and formation of the triple phase boundary.^[46,47] After 10 cycles, maximum discharge capacity attained for CoFe₂O₄@N-CNHs-30% is 280.30 mAh g⁻¹ (DOD 34.20%) and displayed constant behavior for ≈55 cycles. The energy density^[48] calculation reveals that the energy density of the CoFe₂O₄@N-CNHs-30% hybrid cathode (436.45 Wh Kg⁻¹) is higher than that of the other CoFe₂O₄@N-CNH nanohybrids obtained herein and even the standard catalyst 20% Pt/C + RuO₂ (322.30 Wh Kg⁻¹) (Table S6, Supporting Information). The power density of CoFe₂O₄@N-CNHs-30% (503.98 W kg⁻¹) is comparatively higher than other nanohybrids and standard catalyst 20% Pt/C + RuO₂ (Table S6, Supporting Information). Thus, CoFe₂O₄@N-CNHs-30% as air cathode exhibits significantly better electrocatalytic performance and cycling durability compared with the other CoFe₂O₄@N-CNH nanohybrids and the standard 20% Pt/C + RuO₂.

For comparison, we tested a Zinc-air battery with zinc foil as a standard anode utilizing CoFe₂O₄@N-CNHs-30% as air cathode (Figure S13, Supporting Information). The zinc foil-based cell exhibits a maximum discharge capacity of 48.86 mAh g⁻¹ with a DOD of only 5.9% and survives only for 130 h. Thus, zinc-air batteries fabricated with CoFe₂O₄@N-CNHs as cathode catalyst and ZnO/C as anode perform better than zinc-air batteries with zinc foil as an anode. The better performance of this nanohybrid cathode catalyst is mainly attributed to the well-defined N-doped carbon nanohorn structure with evenly dispersed nanosize CoFe₂O₄ particles in the catalyst structure. Aggregation of active species and deterioration of the unique structure seems significantly prevented during repeated charge/discharge procedure. The advantage of CoFe₂O₄@N-CNHs-30% catalyst includes, high energy and power density which indicate it could serve as an economical ORR catalyst for practical and rechargeable zinc-air batteries. Compared to the standard catalyst-based battery, the discharging and charging processes of the CoFe₂O₄@N-CNHs-30% based battery is stable. Small voltage gap of CoFe₂O₄@N-CNHs-30% based battery indicates excellent rate proficiency. Based on the above results, the CoFe₂O₄@N-CNHs-30% catalyst with its excellent activity and durability is promising for rechargeable zinc-air batteries.

To test whether the cycling durability can be improved further a fluorinated CoFe₂O₄@N-CNHs-30% spinel catalyst was evaluated^[6] in order to study the substitutional influence of F⁻ compared to O²⁻ in the spinel lattice. No anticipated improvement is observed in bifunctional activity of the fluorinated sample; more detail is included in supporting information (Figure S14, Supporting Information). Finally, we also followed a classical co-precipitation approach to prepare a functional CoFe₂O₄@CNH catalyst and test its activity (Figure S15, Supporting Information). TEM images of the CoFe₂O₄@CNH composite indicate big chunks of CoFe₂O₄ non-uniformly scattered over the

CNH material (Figure S15a–c, Supporting Information) The obtained CoFe₂O₄@CNHs composite is first tested for its ORR activity (Figure S15d,e, Supporting Information) and finally again as an air electrode catalyst in a zinc-air battery set up (Figure S15f, Supporting Information). However, this catalyst exhibits inferior ORR activity and zinc-air battery durability compared to CoFe₂O₄@N-CNHs-30%.

3. Conclusion

In summary, a series of noble metal-free bifunctional hybrid catalysts, CoFe₂O₄@N-CNH, are successfully fabricated and tested toward its electrochemical performance. The fabrication approach constitutes single-step high-temperature annealing of iron(III) and cobalt(II) urea nitrate complexes tethered onto the surface of CNHs in an Ar/NH₃ atmosphere. The NH₃-based heat treatment of CNHs effectively creates a porous structure by eliminating amorphous carbon and exposing inter- and intranahorn interstices and void space. Combination of urea and NH₃ lead to the N-functionalization of CNHs. TEM studies confirm the homogeneous distribution of CoFe₂O₄ nanoparticles anchored effectively on N-functionalized CNHs. These nanohybrids due to their hierarchical porous framework and large specific surface area exhibit an improved active site exposure and an expedited oxygen and electron transport. The CoFe₂O₄@N-CNHs-30% (30% carbon content) catalyst shows superior ORR kinetics compared to other nanohybrids as well as compared to its individual components CNHs and ferrite alone. It exhibits higher diffusion-limiting current density (−6.51 mA cm⁻²) and comparable half-wave potential compared to a standard material composed of 20% Pt/C. The admirable bifunctional activity of the CoFe₂O₄@N-CNH nanohybrids has been ascribed to the improved performance of the CoFe₂O₄ spinel oxide on CNHs with its higher content of effective N species and the existence of efficient mass transfer channels (voids) due to the ammonia treatment. The CoFe₂O₄@N-CNHs-30% nanohybrid also establishes outstanding OER activity with a lesser overpotential and a smaller Tafel slope than the standard OER catalyst RuO₂. Moreover, using the CoFe₂O₄@N-CNHs-30% electrocatalyst on the cathode side of a zinc-air battery allows a remarkable specific energy density of 436.5 Wh Kg⁻¹ that is significantly higher than that of the other nanohybrids studied and the standard catalyst 20% Pt/C + RuO₂ as well (322.30 Wh Kg⁻¹). The long-term cycling accomplishment of the CoFe₂O₄@N-CNHs-30% cathode catalyst when implemented in a zinc-air battery reveals a decent long-term stability of ≈200 h paired with an excellent specific capacity of 280 mAh g⁻¹ which outperforms the 20% Pt/C-RuO₂ as ORR/OER catalyst in a zinc-air battery. Altogether this study presents an efficient noble metal-free, spinel type nitrogen-doped bifunctional catalyst which certainly enables studies toward further optimization. In addition, the presented straightforward molecular based synthetic approach allows for a development of other spinel type chalcogenides and hybrid catalysts therefrom on a broader experimental scopes.

Supporting Information

Supporting Information is available from the Wiley Online Library or from the author.

Acknowledgements

TEM measurements were recorded at the Ernst-Ruska Center for Microscopy (ERC) at Jülich under contract ERC-TUDA. The authors are grateful to Jörg Engstler for TEM studies and Silvio Heinschke for XRD and BET measurements, † Ildiko Balog and Chandrajett Mohapatra for thermogravimetric measurements and assistance with RDE measurements (all of TUDA). The authors are thankful to N. Molitor (TIE, Griesheim), for providing a sample of carbon nanohorns (CNHs).

Conflict of Interest

The authors declare no conflict of interest.

Data Availability Statement

The data that support the findings of this study are available from the corresponding author upon reasonable request.

Keywords

cobalt ferrite, metal-urea complex, nitrogen doped carbon, oxygen evolution reaction, oxygen reduction reaction, zinc-air battery

Received: May 29, 2024

Published online:

- [1] a) X. Chen, Y. Zhang, C. Chen, H. Li, Y. Lin, K. Yu, C. Nan, C. Chen, *Nano-Micro Lett.* **2023**, *16*, 27; b) X. Xu, K. S. Hui, D. A. Dinh, K. N. Hui, H. Wang, *Mater. Horiz.* **2019**, *6*, 1306; c) W. Wang, Y.-C. Lu, *Acc. Chem. Res.* **2021**, *2*, 515; d) R. Buckingham, T. Asset, P. Atanassov, *J. Power Sources* **2021**, *498*, 229762; e) C.-S. Li, Y. Sun, F. Gebert, S.-L. Chou, *Adv. Energy Mater.* **2017**, *7*, 1700869.
- [2] Y. Li, M. Gong, Y. Liang, J. Feng, J.-E. Kim, H. Wang, G. Hong, B. Zhang, H. Dai, *Nat. Commun.* **2013**, *4*, 1805.
- [3] M. Prabu, P. Ramakrishnan, H. Nara, T. Momma, T. Osaka, S. Shanmugam, *ACS Appl. Mater. Interfaces* **2014**, *6*, 16545.
- [4] J. Zhou, L. Zhang, Y.-C. Huang, C.-L. Dong, H.-J. Lin, C.-T. Chen, L. H. Tjeng, Z. Hu, *Nat. Commun.* **2020**, *11*, 1984.
- [5] I. Kone, Z. Ahmad, A. Xie, L. Kong, Y. Tang, Y. Sun, Y. Chen, X. Yang, P. Wan, *Energy Technol.* **2021**, *9*, 2001117.
- [6] K. Xiao, Y. Wang, P. Wu, L. Hou, Z.-Q. Liu, *Angew. Chem., Int. Ed.* **2023**, *62*, 202301408.
- [7] Y. Wang, R. Gan, H. Liu, M. Dirican, C. Wei, C. Ma, J. Shi, X. Zhang, *J. Mater. Chem. A* **2021**, *9*, 2764.
- [8] a) H. Song, Y. Li, L. Shang, Z. Tang, T. Zhang, S. Lu, *Nano Energy* **2020**, *72*, 104730; b) C. Li, Z. Yu, H. Liu, M. Xiong, *Chem. Eng. J.* **2019**, *371*, 433.
- [9] Z.-C. Yao, T. Tang, J.-S. Hu, L.-J. Wan, *Energy Fuels* **2021**, *35*, 6380.
- [10] Y. Niu, X. Huang, L. Zhao, W. Hu, C. M. Li, *ACS Sustain. Chem. Eng.* **2018**, *6*, 3556.
- [11] C. Wei, Z. Feng, G. G. Scherer, J. Barber, Y. Shao-Horn, Z. J. Xu, *Adv. Mater.* **2017**, *29*, 1606800.
- [12] T. Oh, D. Park, J. Kim, *Int. J. Hydrogen Energy* **2019**, *44*, 2645.
- [13] W. Bian, Z. Yang, P. Strasser, R. Yang, *J. Power Sources* **2014**, *250*, 196.
- [14] V. Kashyap, S. K. Singh, S. Kurungot, *ACS Appl. Mater. Interfaces* **2016**, *8*, 20730.
- [15] V. Kashyap, S. Kurungot, *ACS Catal.* **2018**, *8*, 3715.
- [16] T. Li, Y. Lv, J. Su, Y. Wang, Q. Yang, Y. Zhang, J. Zhou, L. Xu, D. Sun, Y. Tang, *Adv. Sci.* **2017**, *4*, 1700226.
- [17] S. Liu, W. Bian, Z. Yang, J. Tian, C. Jin, M. Shen, Z. Zhou, R. Yang, *J. Mater. Chem. A* **2014**, *2*, 18012.
- [18] S. Iijima, M. Yudasaka, R. Yamada, S. Bandow, K. Suenaga, F. Kokai, K. Takahashi, *Chem. Phys. Lett.* **1999**, *309*, 165.
- [19] J. Y. Jung, S. Kim, J.-G. Kim, M. J. Kim, K.-S. Lee, Y.-E. Sung, P. Kim, S. J. Yoo, H.-K. Lim, N. D. Kim, *Nano Energy* **2022**, *97*, 107206.
- [20] a) S. M. Unni, R. Illathvalappil, S. N. Bhange, H. Puthenpediakkal, S. Kurungot, *ACS Appl. Mater. Interfaces* **2015**, *7*, 24256; b) Y. Guo, Y. Zhou, Y. Nan, B. Li, X. Song, *ACS Appl. Mater. Interfaces* **2020**, *12*, 12743; c) B. Devadas, T. Imae, *Electrochem. Commun.* **2016**, *72*, 135; d) X. Liu, H. Li, F. Wang, S. Zhu, Y. Wang, G. Xu, *Biosens. Bioelectron.* **2010**, *25*, 2194.
- [21] a) C.-M. Yang, Y.-J. Kim, J. Miyawaki, Y. A. Kim, M. Yudasaka, S. Iijima, K. Kaneko, *J. Phys. Chem. C* **2015**, *119*, 2935; b) R. Yuge, S. Bandow, K. Nakahara, M. Yudasaka, K. Toyama, T. Yamaguchi, S. Iijima, T. Manako, *Carbon* **2014**, *75*, 322.
- [22] D. J. Babu, T. Herdt, S. Okeil, M. Bruns, R. Staudt, J. J. Schneider, *J. Mater. Chem. A* **2016**, *4*, 14267.
- [23] a) W. Zhang, X. Yao, S. Zhou, X. Li, L. Li, Z. Yu, L. Gu, *Small* **2018**, *14*, 1800423; b) I. Kone, A. Xie, Y. Tang, Y. Chen, J. Liu, Y. Chen, Y. Sun, X. Yang, P. Wan, *ACS Appl. Mater. Interfaces* **2017**, *9*, 20963.
- [24] J. Y. Jung, J.-H. Jang, J.-G. Kim, K.-S. Lee, H.-K. Lim, P. Kim, R. P. H. Chang, J.-W. Park, S. J. Yoo, N. D. Kim, *Small Methods* **2021**, *5*, 2100239.
- [25] a) K. A. Béres, Z. Homonnay, L. Kótai, *ACS Omega* **2024**, *9*, 11148; b) Y. Qiu, L. Gao, *J. Am. Ceram. Soc.* **2004**, *87*, 352; c) T. Theophanides, P. D. Harvey, *Coord. Chem. Rev.* **1987**, *76*, 237.
- [26] T. Bies, R. C. Hoffmann, M. Stöter, A. Huber, J. J. Schneider, *ChemistryOpen* **2020**, *1251–1263*, 1251.
- [27] N. Li, Z. Wang, K. Zhao, Z. Shi, Z. Gu, S. Xu, *Carbon* **2010**, *48*, 1580.
- [28] S. M. Unni, S. Ramadas, R. Illathvalappil, S. N. Bhange, S. Kurungot, *J. Mater. Chem. A* **2015**, *3*, 4361.
- [29] Y. Zhao, J. Li, Y. Ding, L. Guan, *RSC Adv.* **2011**, *1*, 852.
- [30] D. Kasuya, M. Yudasaka, K. Takahashi, F. Kokai, S. Iijima, *J. Phys. Chem. B* **2002**, *106*, 4947.
- [31] L. Zhao, R. He, K. T. Rim, T. Schiros, K. S. Kim, H. Zhou, C. Gutiérrez, S. P. Chockalingam, C. J. Arguello, L. Pálová, D. Nordlund, M. S. Hybertsen, D. R. Reichman, T. F. Heinz, P. Kim, A. Pinczuk, G. W. Flynn, A. N. Paspurthy, *Science* **2011**, *333*, 999.
- [32] S. M. Unni, S. N. Bhange, R. Illathvalappil, N. Mutneja, K. R. Patil, S. Kurungot, *Small* **2015**, *11*, 352.
- [33] P. Chandramohan, M. P. Srinivasan, S. Velmurugan, S. V. Narasimhan, *J. Solid State Chem.* **2011**, *184*, 89.
- [34] Y. Nan, B. Li, X. Song, N. Sano, *Carbon* **2019**, *142*, 150.
- [35] E. Bekyarova, K. Kaneko, M. Yudasaka, D. Kasuya, S. Iijima, A. Huidobro, F. Rodriguez-Reinoso, *J. Phys. Chem. B* **2003**, *107*, 4479.
- [36] L.-S. Johansson, J. M. Campbell, O. J. Rojas, *Surf. Interface Anal.* **2020**, *52*, 1134.
- [37] R. Azmi, V. Trouillet, M. Strafela, S. Ulrich, H. Ehrenberg, M. Bruns, *Surf. Interface Anal.* **2018**, *50*, 43.
- [38] M. C. Biesinger, B. P. Payne, A. P. Grosvenor, L. W. Lau, A. R. Gerson, R. S. Smart, *Appl. Surf. Sci.* **2011**, *257*, 2717.
- [39] J. Sun, N. Guo, Z. Shao, K. Huang, Y. Li, F. He, Q. Wang, *Adv. Energy Mater.* **2018**, *8*, 1800980.
- [40] Y. Go, K. Min, H. An, K. Kim, S. Eun Shim, S.-H. Baeck, *Chem. Eng. J.* **2022**, *448*, 137665.
- [41] a) W. Wang, H. Wang, Y. Yu, Z. Wu, M. Asif, H. Liu, *Catal. Sci. Technol.* **2018**, *8*, 480; b) Y. Pan, S. Liu, K. Sun, X. Chen, B. Wang, K. Wu, X. Cao, W.-C. Cheong, R. Shen, A. Han, Z. Chen, L. Zheng, J. Luo, Y. Lin, Y. Liu, D. Wang, Q. Peng, Q. Zhang, C. Chen, Y. Li, *Angew. Chem., Int. Ed.* **2018**, *57*, 8614.
- [42] S. Li, C. Cheng, X. Zhao, J. Schmidt, A. Thomas, *Angew. Chem., Int. Ed.* **2018**, *57*, 1856.

- [43] X.-T. Wang, T. Ouyang, L. Wang, J.-H. Zhong, Z.-Q. Liu, *Angew. Chem., Int. Ed.* **2020**, *59*, 6492.
- [44] Y. Wang, J. Wu, S. Tang, J. Yang, C. Ye, J. Chen, Y. Lei, D. Wang, *Angew. Chem., Int. Ed.* **2023**, *62*, 202219191.
- [45] Y. Su, H. Jiang, Y. Zhu, X. Yang, J. Shen, W. Zhou, J. Chen, C. Li, *J. Mater. Chem., A* **2014**, *2*, 7281.
- [46] D. Deckenbach, J. J. Schneider, *J. Power Sources* **2021**, *488*, 229393.
- [47] D. Aasen, M. P. Clark, D. G. Ivey, *J. Electrochem. Soc.* **2020**, *167*, 40503.
- [48] a) M. Sethi, U. S. Shenoy, D. K. Bhat, *Nanoscale Adv.* **2020**, *2*, 4229;
b) H. Jiang, L. Yang, C. Li, C. Yan, P. S. Lee, J. Ma, *Energy Environ. Sci.* **2011**, *4*, 1813.